Magnetization Slow Dynamics in Mononuclear Co(II) Field-Induced Single-Molecule Magnet

Nikoleta Malinová, Jana Juráková, Barbora Brachňaková, Jana Dubnická Midlíková, Erik Čižmár, Vinicius Tadeu Santana, Radovan Herchel, Milan Orlita, Ivan Mohelský, Ján Moncol, et al.

Magnetization Slow Dynamics in Mononclear Co(II) Field-Induced Single-Molecule Magnet

Nikoleta Malinová,[a] Jana Juráková,[b] Barbora Brachňaková,[a] Jana Dubnická Midlíková,[b] Erik Čižmár,[c] Vinicius Tadeu Santana,[b] Radovan Herchel,[d] Milan Orlita,[e] Ivan Mohelský,[e] Ján Moncoľ,[a] Petr Neugebauer,[b] and Ivan Šalitroš[ab*]

a) Department of Inorganic Chemistry, Faculty of Chemical and Food Technology, Slovak University of Technology in Bratislava. Bratislava SK-81237, Slovakia. *e-mail: ivan.salitros@stuba.sk

b) Central European Institute of Technology, Brno University of Technology, Purkyňova 123, 61200 Brno, Czech Republic.

c) Institute of Physics, Faculty of Science, P.J. Šafárik University Park Angelinum 9, 04154 Košice, Slovakia

d) Department of Inorganic Chemistry, Faculty of Science, Palacký University, 17. listopadu 12, 771 46 Olomouc, Czech Republic

e) LNCMI-EMFL, CNRS UPR3228, Univ. Grenoble Alpes, Univ. Toulouse, Univ. Toulouse 3, INSA-T, Grenoble and Toulouse, France

Graphical abstract & Synopsis

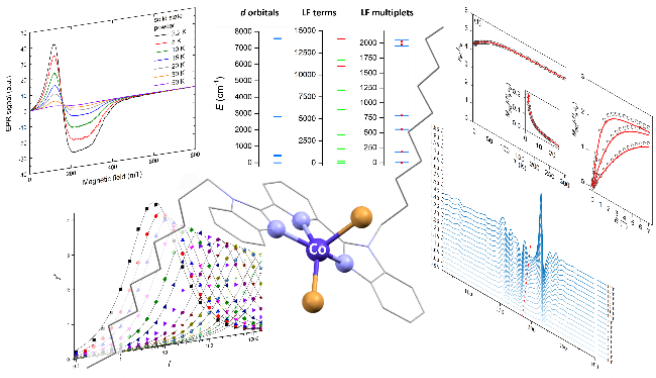

The pentacoordinate field-assisted Co(II) single-molecule magnet was prepared and structurally characterized. The static magnetic properties were analyzed by L-S Hamiltonian and results supported by resonance spectroscopies as well as by theoretical calculations. Field-assisted slow relaxation of magnetization was investigated in detail at variable field and temperature.

Abstract

The novel tridentate ligand L (2,6-Bis(1-(n-decyl)-1*H*-benzimidazol-2-yl)pyridine) was used for the synthesis of mononuclear Co(II) complex **1** of general formula [Co(L)Br_2]. The single-crystal X-ray structural investigation confirmed the expected molecular structure and non-covalent contacts were inspected by Hirschfeld surface analysis. The electronic structure of square-pyramidal complex **1** contains an orbitally degenerate ground state which predetermines to use the Griffith-Figgis Hamiltonian for the analysis of magnetic properties. CASSCF-NEVPT2 calculations along with far-infrared magnetic spectroscopy show excellent agreement with the Griffith-Figgis Hamiltonian parameters obtained from the magnetic investigation. The high and negative value of the axial crystal field parameter Δ_{ax} and the calculated *g*-tensor components suggest the axial magnetic anisotropy of **1**. The low-temperature EPR spectra of the studied compounds were analyzed within a simplified effective spin-1/2 model to determine effective *g*-tensor components of the ground Kramers doublet, which agree with the electronic structure predicted within the CASSCF-NEVPT2 theory. The dynamic magnetic investigation revealed field-induced single-channel slow relaxation of magnetization with maximal relaxation time $\tau \approx 28$ ms at low temperatures. The comprehensive analysis of the field and temperature evolution of τ indicates that all three direct, Raman, and Orbach processes are invovled in slow relaxation of magnetization in **1**.

Introduction

Single-molecule magnets (SMMs) are an exciting example of magnetically bistable molecular units possessing slow magnetic relaxation and have attracted considerable attention due to their potential applications in molecular switches, sensors, high-density information storage, and molecule spintronics.[1][2] The development in this field is currently aimed at obtaining the large energy barriers that helps to retain either one of the two magnetic states for extending the relaxation time.[3] The energy barrier of magnetization reversal (U) depends on the spin ground state (S) and a zero-field splitting (ZFS) of that ground state (D). The height of this barrier is given by $U = S^2|D|$ for integer spin (non-Kramers ions) and $U = (S^2 - 1/4)|D|$ for non-integer spin (Kramers ions).[3]

Contrary to lanthanide SMMs,[4] although the 3*d* orbitals of transition metal ions are valence orbitals and the orbital angular momentum can be readily quenched by ligand fields, transition metal coordination compounds exhibiting slow magnetic relaxation phenomena are at the forefront of the research on nanomagnetic materials.[5] Particular attention has been paid to Co(II) complexes since high-spin Co(II) ion usually exhibits unquenched orbital angular momentum contribution, which is responsible for the significant single-ion magnetic anisotropy.[6-8] In this respect, the majority of reports are focused on the slow relaxation of magnetization (SRM) in tetra-, penta- and hexa-coordinate mononuclear Co(II) complexes.[6] Among them, the pentacoordinate Co(II) complexes with one rigid tridentate *terpy*-like N-donor ligand (*terpy* = 2,6-bis(2-pyridyl)pyridine) and two terminal ligand anions present an exciting family of field induced SMMs, where the correlation between the geometry of coordination polyhedra and the magnetic anisotropy might help to understand the impact of the molecular design on the SRM.[9],[10]

Some of our as well as the other recent studies have been focused on the inspection of magnetic anisotropy and on the SRM in pentacoordinate Co(II) complexes with derivatives of bis(1*H*-benzimidazole)pyridine tridentate ligands (Figure 1).[11-13] Those reports prove that rationalized introduction of substituents on tridentate ligands along with the variation of miscellaneous halido or pseudohalido terminal ligand anions X^- affects the geometry of pentacoordinate coordination polyhedra, which can adopt either trigonal-bipyramidal or square-pyramidal arrangement. The investigation of the magnetic anisotropy in the that family of pentacoordinate Co(II) complexes is, however, not so straightforward. As a matter of fact, most of the studies almost exclusively use the ZFS spin Hamiltonian to analyze the static magnetic properties. The axial (D) and rhombic (E) ZFS parameters bear the physical meaning only if the ground state is orbitally non-degenerate and well separated from the closest excited states.[14] Another option is the Griffith-Figgis Hamiltonian which has been originally designed for octahedral systems possessing (or approaching) orbitally triple-degenerate ground state.[14] Ultimately, however, both approaches allow to render the magnetic anisotropy in pentacoordinate Co(II) systems, which is axial in most of the cases[6] and therefore allows the Orbach mechanism of the SRM to be operative.[11],[12]

In this study, we continue our systematic investigation of pentacoordinate Co(II)-SMMs and report on mononuclear Co(II) complex **1** containing 2,6-bis(benzimidazole-1-yl)pyridine tridentate ligand (L) functionalized with aliphatic n-decyl substituents and two bromido terminal ligand anions (Figure 1). The structural investigation confirmed the expected molecular structure expressed by the formula $[Co(L)Br_2]$ and the near environment of complex molecules in the crystal lattice was investigated by Hirschfeld surface analysis. The high-spin state magnetic behavior of **1** was analyzed by means of L-S Hamiltonian based on Griffith and Figgis concepts, and CASSCF-NEVPT2 theoretical calculations. The low-temperature EPR spectra were analyzed within a simplified effective spin-1/2 model to determine effective *g*-tensor components of the ground Kramers doublet, which are in agreement with the predicted electronic structure. A direct experimental measurement of the separation between the ground and first excited states was obtained with FIRMS spectra, which were also simulated with the Griffith – Figgis Hamiltonian. The dynamic magnetic properties investigation revealed field-induced SRM with a single relaxation channel governed by direct, Raman, and Orbach relaxations.

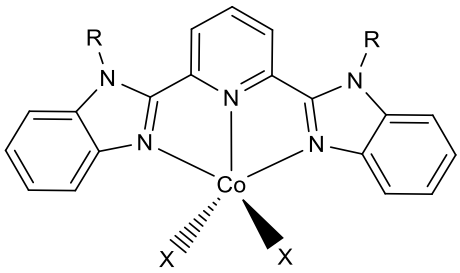

Figure 1 General molecular structure of pentacoordinate Co(II) SMMs with tridentate derivatives of 2,6-bis(benzimidazole-1-yl)pyridine and with halido or pseudohalido terminal ligand anions X^-.

Experimental part

Materials and methods

1-bromdecane p.a., K_2CO_3, dimethylformamide p.a., acetonitrile p.a., dichloromethane p.a., $CoBr_2 \cdot 6H_2O$, and chloroform p.a. were purchased from Sigma-Aldrich or Mikrochem and used as received without any further purification. The starting material 2,6-bis(benzimidazol-2-yl)pyridine was prepared according to the previously reported procedure.[15] IR spectra in the interval from 4000 to 400 cm^{-1} of herein reported compounds were measured on Nicolet 5700 spectrometer (ATR technique). Elemental analysis of carbon, hydrogen and nitrogen was carried out by EA CHNS(O) Flash 1112 machine The NMR spectra were recorded on Bruker DPX 500 spectrometer. The UV-VIS spectra were measured in solid state on Specord 200 spectrophotometer in the range of 800 – 200 nm.

Synthesis

2,2'-(pyridine-2,6-diyl)bis(1-decyl-1H-benzimidazole) (L): 50 ml round-bottom flask was charged with 2,6-bis(benzimidazol-2-yl)pyridine (2 g, 6.42 mmol, 1eq) and dissolved in 15 ml DMF. Then, K_2CO_3 (2.7g, 19.3 mmol, 3 eq) was added into the solution and suspension was stirred for 2 hours at 70°C. 1-bromdecane (3.4 ml, 16.05 mmol, 2.5 eq) was added dropwise over the stirring suspension. The reaction mixture was refluxed at 100°C overnight and cooled down to room temperature. Solvent

was removed by vacuum distillation, the residue was treated with distilled water (50 ml) and extracted with CH_2Cl_2 (3 x 200 ml). The organic solvent was removed using a rotary evaporator and the oily residue was column chromatographed on silica gel with $CHCl_3$/ethyl acetate (5:1) as an eluent. The main product L was isolated as first fraction (R_f = 0.61 in $CHCl_3$:ethyl acetate = 3:4) in 42 % yield (0.6 g, 0.71mmol) as orange oily liquid. The minor side-product of this reaction – 2-[6-(1H-benzimidazol-2-yl)pyridin-2-yl]-1-methyl-1H-benzimidazole (L_m) was collected as the second and more polar fraction (R_f = 0.27 in $CHCl_3$:ethyl acetate = 3:4) in 25 % yield (0.1 g, 0.15 mmol) form as beige powder. Ligand L: IR (ATR, $\tilde{\upsilon}$ / cm^{-1}): 3090 (w, C_{ar}-H), 2921 (s, ν_{as}(C_{al}-H), 2852 (s, ν_s(C_{al}-H), 1572 (m, C_{ar}-C_{ar}, C_{ar}-N), 1463, 1436 (s, C_{ar}-C_{ar}, C_{ar}-N), 1413 (m, δ_{as}(C_{al}-H), 1330 (m, δ_s(C_{al}-H). UV – VIS (acetonitrile, λ / nm): 215 (π→π*), 320 (n→π*). ^{1}H NMR (300 MHz, $CDCl_3$, 25 °C, δ / ppm): 8.32 (d. 2H. J_1 = 7.9 Hz), 8.06 (m. 1H), 7.87 (dd. 2H. J_1= 9.5 Hz, J_2= 0.5 Hz), 7.45 (d. 2H, J_1 = 1.2 Hz), 7.35 (m. 4H), 4.7 (t, 4H, J_1 = J_2 = 7.3 Hz), 3.63 (m, 4H), 1.73 (m, 4H), 1.55 (m, 4H), 1.06 (m, 18H), 0.88 (t, 6H, J_1 = 6.6 Hz, J_2 = 7.1 Hz). ^{13}C NMR (75 MHz, $CDCl_3$, 25 °C, δ / ppm): 150.31 (C), 150.09 (C), 142.92 (C), 138.24 (CH), 136.38 (C), 125.59 (CH), 123.59 (CH), 122.84 (CH), 120.44 (CH), 110.46 (CH), 45.04 (CH_2), 32.97 (CH_2), 31.89 (CH_2), 29.75 (CH_2), 29.69 (CH_2), 29.45 (CH_2), 29.31 (CH_2), 25.90 (CH_2), 22.74 (CH_2), 14.24 (CH_3). Ligand L_m: Elemental analysis for $C_{29}H_{33}N_5$ (M_r = 451.606 g / mol): exp. (calc.) C = 77.99 % (77.13 %), H = 7.46 % (7.37 %), N = 14.98 % (15.51 %). IR (ATR, $\tilde{\upsilon}$ / cm^{-1}): 3051 (w, C_{ar}-H). 2922 (s, ν_{as}(C_{al}-H), 2851 (s, ν_s(C_{al}-H), 1594 (m, C_{ar}-C_{ar}, C_{ar}-N), 1569, 1465, 1442 (s, C_{ar}-C_{ar}. C_{ar}-N), 1419 (s, δ_{as}(C_{al}-H), 1331 (m, δ_s(C_{al}-H). UV – VIS (acetonitrile, λ / nm): 204 (π→π*), 323 (n→π*).^{1}H NMR (300 MHz, $CDCl_3$, 25 °C, δ / ppm): 13.17 (s, 1H), 8.14 (d, 1H, J_1 = 7.9 Hz), 8.01 (m, 1H), 7.88 (m, 2H), 7.83 (m, 1H), 7.6 (t, 1H, J_1 = J_2 = 7.9 Hz), 7.44 (m, 4H), 7.14 (m. 1H), 3.79 (t, 2H, J_1 = J_2 = 7.4 Hz), 1.36 (m. 2H), 1.12 (m. 6H), 0.96 (m. 8H), 0.82 (t, 3H, J_1 = 6,9 Hz, J_2 = 7.2 Hz). ^{13}C NMR (75 MHz, $CDCl_3$, 25 °C, δ / ppm): 151.49 (C), 150.80 (C), 150.08 (C), 148.53 (C), 145.03 (C), 143.00 (C), 138.19 (CH), 136.26 (C), 135.46 (C), 125.55 (CH), 124.41 (CH), 123.76 (CH), 123.56 (CH), 123.17 (CH), 122.29 (CH), 120.72 (CH), 120.22 (CH), 112.14 (CH), 111.59 (CH), 44.37 (CH_2), 32.29 (CH_2), 30.23 (CH_2), 29.85 (CH_2), 29.68 (CH_2), 29.44 (CH_2), 27.03 (CH_2), 23.14 (CH_2), 14.63 (CH_3).

Complex **1** ([Co(L)Br_2]): $CoBr_2 \cdot 6H_2O$ (78 mg, 0.339 mmol, 1 eq) was dissolved in 5 ml of acetonitrile and added into the acetonitrile solution (30 ml) of ligand **L** (200 mg, 0.338 mmol, 1eq). When the solution of Co(II) salt was added, the yellow to green color change occurred immediately without the the precipitation. Reaction mixture was refluxed for 3 hours, filtered off and mother liquor was slowly crystallized at room temperature in order to grow single crystals suitable for the diffraction analysis.. The green crystals of **1** were collected by filtration after several days. Yield 34% (49 mg, 0.06 mmol). Elemental analysis for $C_{35}H_{45}Br_2CoN_5$ (M_w = 810.62 g mol^{-1}) found % (expected %): C 56.99 (57.79); N 8.59 (8.64); H 6.43 (6.59). FT−IR (ATR, $\tilde{\nu}_{max}$/cm^{-1}): 3053, 3018 (m, ν(C_{ar}-H)); 2917, 2580 (m, ν(C_{al}-H)); 1598, 1573 (m, ν(C_{ar}-C_{ar}) or ν(CN)). UV-VIS (nujol, λ/nm): 196, 219, 244, 311, 348.

X-ray crystallography and Hirshfeld surface analysis

Data collection and cell refinement of **1** were carried out using Stoe StadiVari diffractometer using Pilatus3R 300K HPAD detector. Xenocs Genix3D Cu HF (microfocused sealed tube, λ = 1.54186 Å) has been used as an X-ray source. The multi-scan absorption corrections were applied using the program Stoe LANA software.[16] The diffraction intensities were corrected for Lorentz and polarization factors. The structure was solved using Superflip program and refined by the full-matrix least-squares procedure with ShelXL (version 2018/3).[17][18] Geometrical analyses were performed with ShelXL. The structure was drawn with OLEX2 software package.[19]

The software CrystalExplorer[20] (version 21.5) was used to calculate Hirshfeld surface,[21],[22] electrostatic potentials[23] and associated fingerprint plots.[24],[25],[26] The Hirshfeld surfaces have been calculated including all orientations of the disordered molecules with their partial occupancies.

Magnetic measurements

Herein reported magnetic investigation have been carried out on MPMS SQUID XL-7 (Quantum design Inc., San Diego, CA, USA). The exact amount of sample was mixed with melted eicosane and filled into the gelatin capsule, which has been used as the sample holder. In the case of magnetic experiments at a static magnetic field (DC), the temperature dependency was recorded in the thermal range 1.9 – 300 K at B = 0.1 T using the 1 K/min sweeping rate, and field-dependency was measured at isothermal conditions in the range B = 0 – 7 T. Collected data were corrected for the diamagnetism of eicosane and gelatin capsule as well as for the molecular diamagnetic contribution, which was calculated using the Pascal constants.[27] Magnetic functions were transformed into the μ_{eff} vs T and M_{mol} vs B dependencies. The experimental details about the magnetic experiments at AC magnetic field are given in the S7 section (vide infra).

Computational details

The electronic structure and magnetic properties of **1** were addressed by the multireference calculations based on the state average complete active space self-consistent field (SA-CASSCF)[28] wave function method complemented by N-electron valence second-order perturbation theory (DLPNO-NEVPT2)[29] were conducted with an ORCA 5.0 computational package.[30] The experimental molecular structure was utilized, in which the positions of hydrogen atoms were normalized with Mercury software.[31] The ZORA relativistic approximation[32] was applied together with ZORA-def2-TZVPP for Co, ZORA-def2-TZVP for N and Br atoms, and ZORA-def2-SVP for C and H atoms.[33] The SARC/J[34] and AutoAux[35] procedure was used for auxiliary basis set together with the chain-of-spheres (RIJCOSX) approximation to exact exchange[36],[37] to speed up the calculations. The active space was defined by seven electrons in five d-orbitals of Co^{II} (CAS(7e,5o)), and all possible multiplets, 10 quartets and 40 doublets, were involved in the calculations. Afterward, the ab initio ligand field theory (AILFT)[38][39] was applied to calculate the splitting of *d*-orbitals (see part S4).

EPR spectroscopy

The spectra of electron paramagnetic resonance (EPR) were studied using Bruker ELEXSYS II E500 X–band spectrometer with an operating frequency of 9.4 GHz equipped with ESR910 helium flow–type cryostat. The measurements were performed in the temperature range from 2 K up to 100 K (since above 50 K the signal is very weak, broad, and featureless, only data below 50 K are reported). The pulverized polycrystalline sample was embedded in Apiezon® N vacuum grease and attached to the Suprasil sample holder. The frozen solution measurements were performed in Wilmad® Suprasil 727-SQ-250M EPR tube using a solution of 5 mg of **1** in 500, 2500, and 7500 mg of acetonitrile (no difference between the spectra for various concentrations was observed).

Far Infrared Magnetic Spectroscopy (FIRMS)

The magneto-optical response of the studied compound has been also explored in the THz/infrared range, using the standard Faraday configuration (i.e. in transmission mode, with the magnetic field parallel to the wave vector of the probing radiation). To ensure transparency in this spectral range, the compounds were mixed with eicosane in the indicated ratio and subsequently pressed into pellets. To measure magneto-transmission, the radiation of a globar, or alternatively, of a mercury lamp, has been analyzed by the Vertex 80v Fourier-transform spectrometer, and using light-pipe optics, delivered to the pellet placed inside a superconducting coil and kept in the helium heat-exchange gas at $T = 4.2$K. After passing through the pellet, the radiation was detected using a composite bolometer placed just below.

Results and discussion

Synthesis and structural investigation

The tridentate ligand L was prepared by nucleophilic substitution of 2,6-bis(1H-benzimidazole-2-yl)pyridine with n-decylbromide in 42 % yield (see Experimental part). The purification of L was impeded by the presence of monosubstituted side product L_m, which was isolated as the second more polar fraction from column chromatography in 25 % yield. Complex **1** was prepared by coordination of L with $CoBr_2.6H_2O$ in acetonitrile and the single crystals were grown by controlled evaporation of mother liquor. The compound crystallizes in the triclinic *P*-1 space group and the asymmetric unit is formed by one solvent-free molecule $[Co(L)Br_2]$ (Figure 2a, Table S1). At 100 K, bond distances of coordination polyhedra indicate the high-spin state of the Co(II) central atom (Table S2). The shortest bond length is formed with pyridine N donor atom, while the longest bonds are with bromido terminal ligands (d_{avg}(Co-Br)=2.45 Å). The coordination polyhedron adopts the shape of a deformed tetragonal pyramid (Table S2) with a basal plane created by three nitrogen and Br1 donor atoms. The central atom is pulled inside the body of the pyramid at a distance 0.534(6) Å from the basal plane.

The crystal structure contains several non-covalent synthons formed between aromatic moieties of neighboring complex molecules, which cause the formation of 1D chain along the *a*-*b* plane (Figure S6). Hirshfeld surface analysis was used to inspect the intermolecular interactions of the crystal

structure of **1**. 3D Hirshfeld surfaces plotted over d_{norm} are shown as transparent to visualize the molecular moiety around which they were calculated (Figure 2b). The deep red spots on the d_{norm} Hirshfeld surfaces indicate the close-contact interactions, which are mainly responsible for the significant intermolecular hydrogen bonding C-H···Br/Br···H-C and H···H (Figure S7) interactions covering 12.0% and 70.9% of the total Hirshfeld surface, respectively. The further less abundant noncovalent contacts are identified between H···C/C···H and aromatic carbon atoms C···C cover 9.12% and 3.0% of the total Hirshfeld surface, respectively.

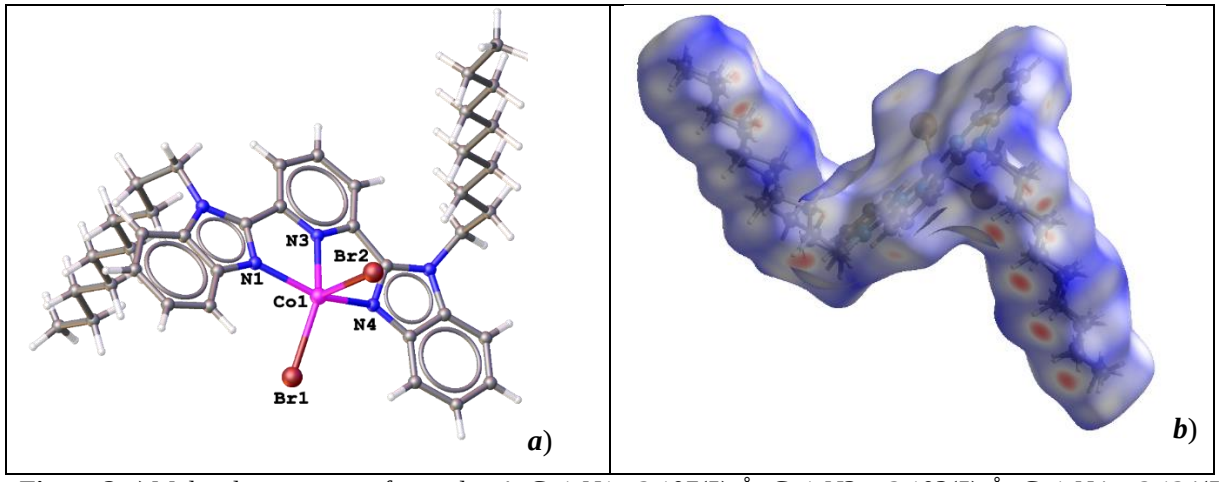

Figure 2 ***a***) Molecular structure of complex **1**; Co1-N1= 2.107(5) Å, Co1-N3 = 2.103(5) Å, Co1-N4 = 2.124(5) Å, Co1-Br1 = 2.443(1) Å, Co1-Cl2 = 2.461(1) Å, τ_5=0.04. ***b***) View of the three-dimensional Hirshfeld surface of **1** plotted over d_{norm} in the range -0.4533 to 1.4113 a.u.

Magnetic characterization of **1** at the static magnetic field was examined in the temperature range 2-300 K at B_{DC} = 0.1 T (μ_{eff} vs T; Fig. 2 left) and in the field range B_{DC} = 0-7 T at three temperatures 2 K, 5 K and 10 K (M_{mol} vs B; Fig. 2 right). The room temperature value μ_{eff} = 5.31 μ_B is significantly higher than the spin-only value for the S = 3/2 system (3.87 μ_B) suggesting a considerable contribution of angular momentum to the overall magnetization. On lowering the temperature, the μ_{eff} obeys Curie law up to ca 100 K and then the presence of ZFS causes a gradual decrease down to 4.4 μ_B at 2 K. Molar magnetization M_{mol} at 7 T and 2 K acquires lower values (2.63 μ_B) than expected for a Curie paramagnet with S = 3/2 (3 μ_B), which indicates notable magnetic anisotropy.

The splitting of S = 3/2 ground state causing the magnetic anisotropy is predominantly treated with the spin Hamiltonian comprising the ZFS and Zeeman terms.[40] However, pentacoordinate Co^{II} complex with the coordination polyhedron close to the square-pyramidal arrangement implies an orbitally degenerate ground state and therefore the spin Hamiltonian is inappropriate as also supported by *ab initio* calculations (*vide infra*). Thus, the DC magnetic data were analyzed with the L-S Hamiltonian based on Griffith and Figgis works[41]–[43] describing the splitting of the $^4T_{1g}$ term originating from the ^4F atomic term in lower symmetries than O_h as follows

$$\hat{H} = -\alpha \cdot \lambda\left(\vec{S}\cdot\vec{L}\right) + \Delta_{ax}\left(\hat{L}_z^2 - \hat{L}^2/3\right) + \Delta_{rh}\left(\hat{L}_x^2 - \hat{L}_y^2\right) + \mu_B\vec{B}\left(g_e\vec{S} - \alpha\vec{L}\right) \qquad (1)$$

The $^4T_{1g}$ splitting is quantified by Δ_{ax} and Δ_{rh} parameters, α is an orbital reduction factor, λ is a spin-orbit coupling parameter and $g_e = 2.0023$. Here, the T_1-P isomorphism is employed, where the angular orbital momentum L adopts the value of **1** with the effective Lande g-factor, $g_L = -1$. The Hamiltonian acts on $|S, L, M_S, M_L>$ base functions with $M_L = 0$, ± 1 and $M_S = \pm 1/2$, $\pm 3/2$.[44] Subsequently, the orbital reduction factor α represents two parameters, $\alpha = A\kappa$, where A is the Figgis coefficient of the configuration interaction resulting from the admixture of the excited terms reflecting the ligand field strength, and κ describes the lowering orbital contribution due to the covalency of the metal-ligand bond. Moreover, the spin-orbit coupling parameter λ can be reduced in comparison with its free-ion value $\lambda_0 = -180\,cm^{-1}$ for Co^{II}, which is attributable to the covalent character of the donor-acceptor bond. With the Hamiltonian in Eq.1 explained, we can proceed with the DC magnetic data analysis. Herein, both temperature and field-dependent magnetic data were fitted together with the help of a program POLYMAGNET.[45] The reasonably good fit was achieved with the following parameters: $\alpha = 2.16$, $\Delta_{ax} = -1503\,cm^{-1}$, $\Delta_{rh} = -270\,cm^{-1}$ and $\lambda = -105\,cm^{-1}$ (Figure 2, Table 1). The negative value of the parameter Δ_{ax} reflects the easy axis type of magnetic anisotropy as visualized in the 3D plots of molar magnetization (Figure S8a). Also, the respective energy levels in the zero magnetic field are plotted in Figure S8b. The energy separation between the ground state and the first excited Kramers doublet is $145\,cm^{-1}$. Within spin Hamiltonian formalism, this energy difference would be equal to $|2D|$ leading to the estimation of $|D| \approx 73\,cm^{-1}$. However, a set of two other excited located at 705 and $906\,cm^{-1}$ Figure S8b excludes the application of the ZFS terms in spin Hamiltonian and reflects the splitting of E-term expected for the ideal square-pyramidal geometry of Co^{II} complexes.

The electronic structure and magnetic properties of **1** were analyzed by the *ab initio* calculations (see Experimental part for more details). The calculated splitting of *d*-orbitals for **1** resembles the pattern calculated for model compound $[CoBr_5]^{3-}$ of ideal square pyramid geometry with C_{4v} symmetry (square pyramidal shape SPY-5, Tab.S2). In such ligand field, the *d*-orbitals are ordered as d_{xy}, (d_{yz}, d_{xz}), d_{z2} and d_{x2-y2}, however, in **1**, the degeneracy of d_{xz} and d_{yz} orbitals is removed due to the symmetry lowering (Figure 3; *left*). Generally, $3d^7$ electronic configuration of Co^{II} ion results in ^4F atomic term, which is split in octahedral ligand field (LF) into $^4T_{1g}$, $^4T_{2g}$ and $^4A_{2g}$ LF terms. Further reducing of the symmetry to square pyramidal C_{4v} symmetry splits $^4T_{1g}$ term to ^4E and $^4A_2$ terms (Figure 3; *middle*, SPY-5). The real LF symmetry in **1** produced splitting of ^4E term to two terms separated by only $244\,cm^{-1}$ and the third term is located at $1616\,cm^{-1}$ (Figure 3; *middle*). The spin-orbit coupling acting upon these lowest three ligand field terms formed six lowest Kramers doublets spanning energy interval 0-$2048\,cm^{-1}$ (Figure 3; *right*).

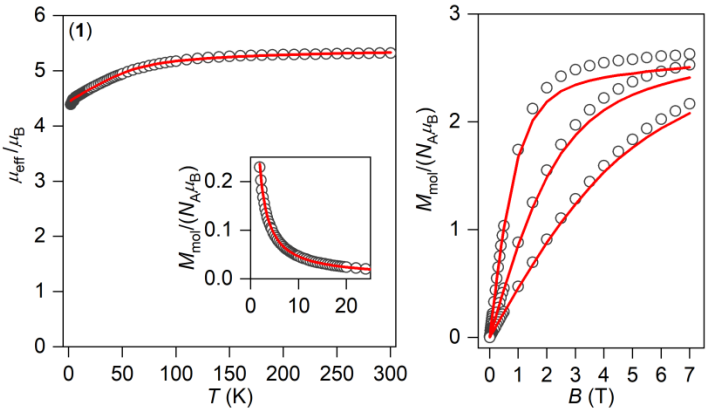

Figure 2. The DC magnetic data for **1** showed as the temperature dependence of the effective magnetic moment and isothermal molar magnetization measured at T = 2, 5 and 10 K. The empty symbols represent the experimental data; the full lines represent the fitted data using Eq.1 with the Hamiltonian parameters listed in the text.

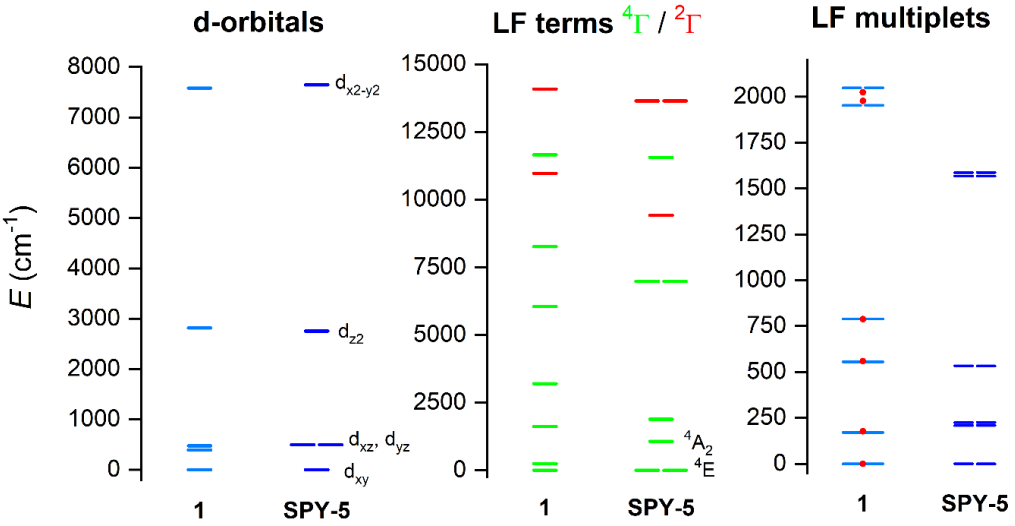

Figure 3 The outcome of the CASSCF/NEVPT2 calculations for complex **1** compared to the ideal spherical square pyramid geometry (SPY-5) of $[CoBr_5]^{3-}$. Plot of the d-orbitals splitting calculated by *ab initio* ligand field theory (AILFT) (*left*), low-lying ligand-field terms (LFT) (*middle*), and ligand-field multiplets (LFM) (*right*). Note: different multiplicities of LFT are shown in a different color. Red full circles in LFM plot represent fit to Eq.1 with parameters listed in the text.

Next, the energies of the six lowest Kramers doublets were used for the analysis of the parameters of the L-S Hamiltonian in Eq.1. Such procedure we already applied for the investigation of several Co^{II} compounds.[46]-[50] The good agreement with the CASSCF/DLPNO-NEVPT2 energy levels was found for Δ_{ax} = -1508 cm^{-1}, Δ_{rh} = -164 cm^{-1}, $\alpha\cdot\lambda$ = -223 cm^{-1} (Table 1). Recently, this procedure was shifted further in order to decipher also values of α and λ separately.[50] Thus, temperature- and field-dependent magnetization data were calculated directly in an ORCA package resulting from CASSCF/DLPNO-NEVPT2 calculations. In the next step, these magnetic data were fitted to Eq.1, but with fixed values of $\alpha\cdot\lambda$, Δ_{ax}, Δ_{rh}, which enabled the determination of α = 1.86 and λ = -120 cm^{-1}, as listed in Table 1. The respective fit is depicted in Figure S9. These values are also in accordance with parameters found by fitting the experimental magnetic data.

Table 1 Parameters of Griffith-Figgis Hamiltonian (Eq.1) for **1** obtained by various approaches

	Magnetic measurements	**CASSCF/DLPNO-NEVPT2**	**FIRMS**
α	2.16	1.86	2.19
Δ_{ax} / cm^{-1}	-1503	-1508	-1508
Δ_{rh} / cm^{-1}	-270	-164	-164
λ / cm^{-1}	-105	-120	-105

As already discussed, a negative value of Δ_{ax} designates the axial type of the magnetic anisotropy, which is also confirmed by the analysis of the lowest Kramers doublet for the effective spin ½ providing *g*-tensor values $g_x = 1.44$, $g_y = 2.26$, $g_z = 8.20$ visualized in Figure 4a. We must also notice that the effective Hamiltonian theory[51] was also applied to CASSCF/DLPNO-NEVPT2 calculations to derive the parameters of the spin Hamiltonian for $S = 3/2$, which resulted in $D = -76.0\,\text{cm}^{-1}$, $E/D = 0.287$. However, the norms of the projected states were 0.644 and 0.811, thus significantly smaller than 1 making the effective Hamiltonian irrelevant. As the single-molecule magnets are defined by the spin reversal energy barrier, the SINGLE_ANISO module[52] was employed and the *ab initio* magnetization blocking barrier was evaluated as depicted in Figure 4b (dashed lines refer to (temperature assisted) quantum tunnelling (blue), Orbach/Raman mechanisms (red) and direct/Raman mechanisms (green).[53] The corresponding matrix element of the transversal magnetic moment between the ground states with opposite magnetization adopted the value of 0.62, thus it is larger than 0.1, which suggests a large predisposition for the quantum tunnelling of magnetization. Indeed, the AC susceptibility measurements confirmed the necessity to apply a static magnetic field to suppress this relaxation pathway. The calculated energy barrier *U* is 170 cm^{-1} for **1**, but usually, the U_{eff} found by analysis of AC data is smaller for Co^{II} SMMs than expected values based on analysis of DC magnetic data or *ab initio* calculations.[54],[55]

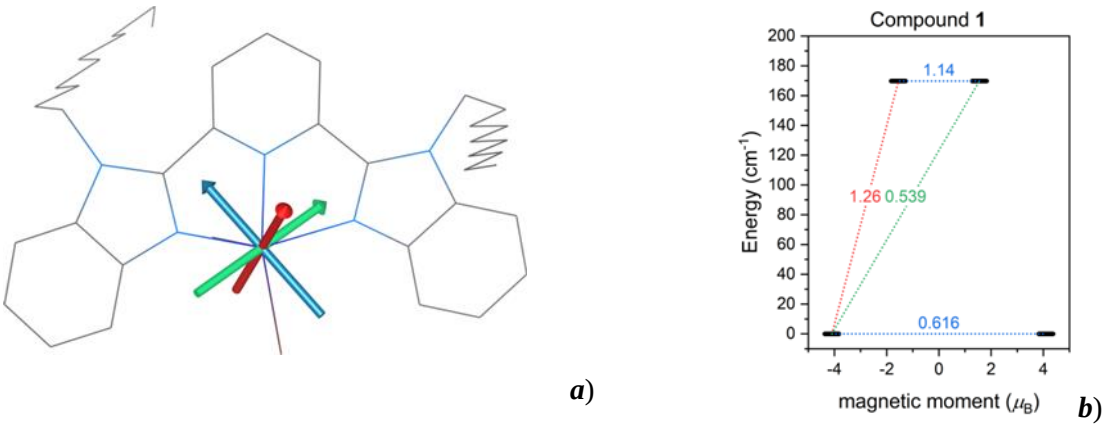

Figure 4. The outcome of CASSCF/DLPNO-NEVPT2 calculations: ***a***) the molecular structure of **1** overlaid with *g*-tensor axis calculated for the lowest Kramers doublet with the effective spin 1/2 (red/green/blue vectors represent $g_x/g_y/g_z$). ***b***) *ab initio* magnetization blocking barrier. The numbers presented in the plots represent the corresponding matrix element of the transversal magnetic moment (for values larger than 0.1 an efficient relaxation mechanism is expected).

The X-band EPR spectra of **1** were measured using a solid-state powdered sample and frozen solution in acetonitrile down to 2.2 K. The temperature evolution of the EPR spectra (Figure S10 and

S11) shows a typical decrease of the signal intensity accompanied by line broadening with increasing temperature for Co(II) complexes with a large energy gap between the ground and first-excited Kramers doublet. In such case, a simplified effective spin-1/2 model describing only the ground Kramers doublet can be used for the analysis yielding highly anisotropic effective *g*-factors. The solid-state EPR spectra in Figure 5 show a substantial line broadening even at the lowest temperatures unable to correctly subtract *g*-factors. Thus, the frozen solution spectra were analyzed within the EasySpin Toolbox[56] including hyperfine interaction and an anisotropic convolutional broadening ΔB (full-width at half-height). Even in the solution, only one of the components of the anisotropic hyperfine coupling parameter *A* was clearly identified in the experimental EPR spectra, but this allows a very accurate estimation of the corresponding *g*-factor component. The best agreement between the simulated and experimental spectra was obtained for a set of effective *g*-factor components $g_1 = 1.975$, $g_2 = 4.55$, and $g_3 = 8.0$, hyperfine coupling components $A_1 = 380\,\text{MHz}$, $A_2 = 170\,\text{MHz}$, and $A_3 = 900\,\text{MHz}$ with $\Delta B_1 = 12\,\text{mT}$, $\Delta B_2 = 25\,\text{mT}$, and $\Delta B_3 = 120\,\text{mT}$. Note that the inaccuracy in the estimation of g_3 and A_3 parameters may be relatively high due to excessive line broadening ($1/g$ dependent as discussed in ref.(57)) in the low field region of the spectra. An average value of the effective *g*-factor $g_{avg} \approx 5.35$ yields a low-temperature value of the magnetization $M_{sat} \approx 2.68\, N_A \mu_B$ within the effective spin-1/2 model, where the experimental magnetization at 2 K tends to saturate (Figure 2). Using Griffith-Figgis formalism, for simple geometry as D_{4h}, a very high value of one of the effective *g*-factors and another $g < 2$ would suggest the presence of the easy-axis magnetic anisotropy. A large difference between the *g*-factor components suggests a significant rhombic anisotropy in **1**. The results of the Angular Overlap model[58] for lower symmetries like a vacant octahedron (C_{4v}) and further deformation into trigonal bipyramid (D_{3h}) yield quite complicated behavior of effective *g*-factor components depending on minor coordination changes. In this case, the shift of the central ion from the base of the vacant octahedron, as suggested for **1,** in a model CoA_5-type of coordination changes the electronic ground state from orbital doublet ^4E (spin Hamiltonian not applicable, this is the ground state term predicted for **1** from CASSCF/DLPNO-NEVPT2 calculations) to orbital singlet $^4A'_2$ (possible to describe using the spin Hamiltonian with $D > 0$). This seems to be compatible with the prediction of the LF terms scheme obtained from CASSCF/DLPNO-NEVPT2 calculations. However, experimental values of the two lower *g*-factor components do not reach the theoretical predictions obtained within quasi-degenerate perturbation theory similar to our previous study.[11] In fact, for the average angle ~103° defining the shift of the central ion from the basal plane of the vacant octahedron in **1**, the effective *g*-factor components close to the ones observed in X-band EPR were obtained within the Angular Overlap model, including the hyperfine coupling parameters. It should be noted that the spin-Hamiltonian formalism does not allow us to estimate the value of the *D* parameter for large values as predicted for **1** even for high-field EPR. In addition, spin-Hamiltonian formalism is not meaningful for easy-axis anisotropy in the case of Co(II) ions, but it is often used to obtain an estimate of the anisotropy parameters.

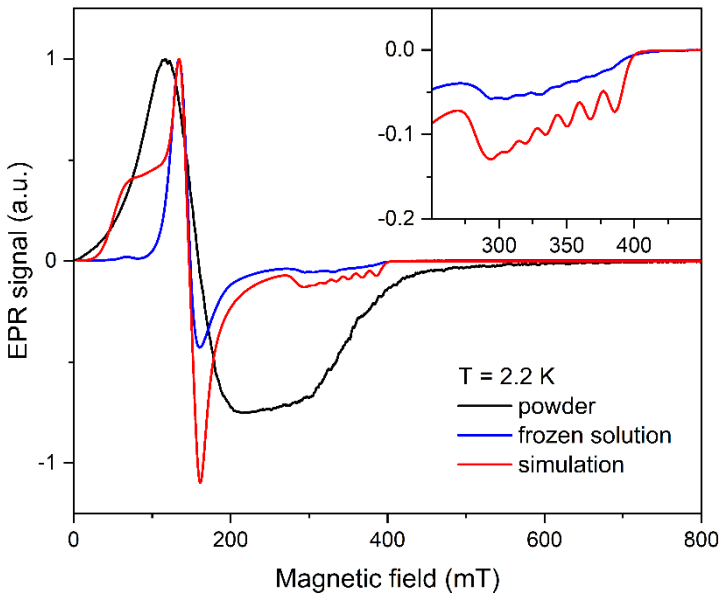

Figure 5 The X-band EPR spectra of **1** were measured at 2.2 K using a solid-state powdered sample (black line) and frozen solution in acetonitrile (blue line). Simulation (red line) includes anisotropic effective g-factors, hyperfine coupling, and anisotropic line broadening within the effective spin-½ model as described in the text.

To determine experimentally the separation between the ground and first excited states, FIRMS was exploited. It enables us to observe EPR transitions of SMMs with large zero-field splitting, mainly based on transition metal complexes. In the case when the system cannot be modeled by SH, we determine the separation between the ground and first excited states directly from the spectra based on the solution of the Griffith – Figgis Hamiltonian. The FIRMS spectra were recorded for pressed powder pellets of **1** (diluted in eicosane) at $T = 4.2$ K, and magnetic fields up to 16 T (Figure S12). The spectra were normalized by the zero-field transmission spectra, T(0), and their corresponding reference transmission spectra, R(0). Normalized transmission spectra were then depicted in the form of a color map for better identification of the EPR transitions. In the color map, the tendency toward the yellow color means the absorption is suppressed by the magnetic field, whereas the dark blue color corresponds to the absorption induced by the magnetic field.

A color map of the normalized FIRMS transmission spectra of complex **1** (Figure 6) shows a clear field-dependence of the peak occurring at ~186 cm^{-1} at zero magnetic field and attributed to the EPR transition between the ground state and the first excited Kramers doublet (transmission spectra at given magnetic fields can be found in Figure S12). FIRMS simulations, shown as dotted lines (Figure 6), were calculated by means of the EasySpin Toolbox for Matlab[43] based on the Griffith – Figgis Hamiltonian and the parameters obtained from magnetization measurement and *ab initio* calculations as an initial guess for the fitting. The red color of the simulation represents the strongly allowed transitions; the grey color indicates forbidden/weakly allowed transitions. We obtained a reasonably good fit with the following parameters: $\Delta_{ax} = -1508\ cm^{-1}$, $\Delta_{rh} = -164\ cm^{-1}$, $\lambda = -105\ cm^{-1}$, $\alpha = 2.19$ (Table

1) which are highly comparable with the values obtained from the analysis of the static magnetic properties or from the CASSCF/DLPNO-NEVPT2 calculations.

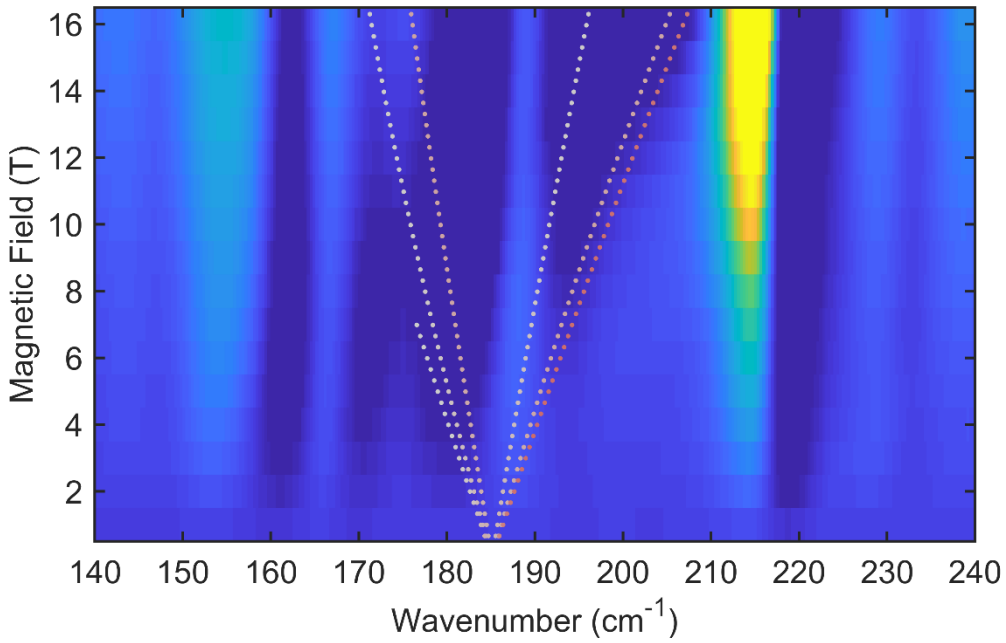

Figure 6 A color map of normalized FIRMS transmission spectra recorded on pressed powder pellets of complex **1** measured at $T = 4.2$ K and magnetic field up to 16 T. The spectra were normalized by zero-field transmission spectra and corresponding reference transmission spectra. Simulations with the Griffith – Figgis Hamiltonian ($\Delta_{ax} = -1508\ cm^{-1}$, $\Delta_{rh} = -164\ cm^{-1}$, $\lambda = -105\ cm^{-1}$, $\alpha = 2.19$) are shown as dotted lines. The red color represents the strongly allowed transitions; the grey color indicates forbidden/weakly allowed transitions. The tendency toward the yellow color means the absorption is suppressed by the magnetic field, whereas the dark blue color corresponds to the absorption induced by the magnetic field.

To probe the SMM behavior in **1**, the alternating-current (AC) susceptibility was measured at low temperatures (see ESI for a detailed experimental description of AC susceptibility measurements and data analysis). At 2 K, static DC field scan revealed the absence of out-of-phase signal χ'' at B = 0 T (Figure S13, Table S4), which is a consequence of the fast relaxation of magnetization resulting from quantum tunnelling effect induced by hyperfine interactions with the nuclear spins. However, the applied static field suppressed the tunnelling, and this allowed to map the SRM at static magnetic fields in the range 0 - 1 T. The frequency-dependent in-phase χ' and out-of-phase χ'' components of AC susceptibility were satisfactorily fitted to the extended one-set Debye model (Figure 7a, equations S1 and S2, see ESI), by which the isothermal χ_T and adiabatic χ_S susceptibilities along with the relaxation time τ and its distribution parameter α were determined at given static magnetic fields (Table S4). In the next step, the evolution of relaxation times τ in static field τ vs B was analyzed with respect to the combination of direct and Raman relaxation mechanisms according to the equation (2)[59]

$$\frac{1}{\tau} = aTH^m + d\left(\frac{1+eH^2}{1+fH^2}\right)T^n \qquad (2)$$

The high-accuracy analysis could be obtained by fitting the low-field part of τ vs B curve (< 0.2 T at 2 K) with the parameters of direct and Raman mechanisms $a = 3624(266)\ T^{-m}\ K^{-1}\ s^{-1}$, $m = 2.68(5)$ and $e = 618(80)\ K^{-2}$, $f = 1117(126)\ K^{-2}$, $2^n d = 59.6(5)\ s^{-1}$, respectively (Figure 7b, red solid line; Table S8). Exponent m is notably lower as expected $m = 4$ for the Kramers systems and fixing this value led to unreliable fits, therefore m was considered as a free parameter. Analysis of τ vs B dependency in the whole range of the applied static field (0.01 T - 1 T) with the fixed Raman parameters from the previous low-field fit afforded more reliable parameters of the direct process $a = 11026(51)\ T^{-m}\ K^{-1}\ s^{-1}$ and $m = 3.32(3)$ (Figure 7b, blue solid line; Table S8).

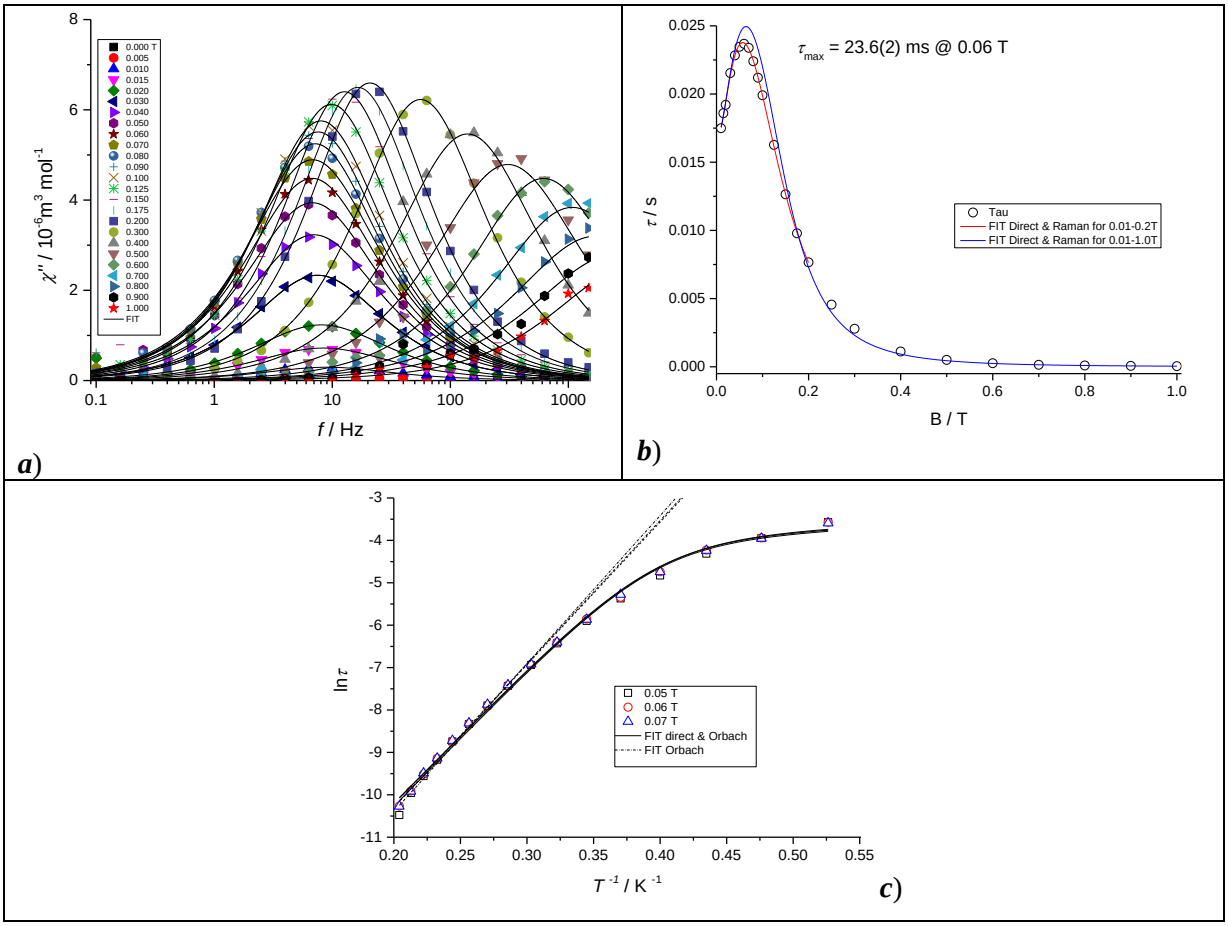

Figure 7 ***a***) Out-of-phase χ'' component of AC susceptibility recorded at 2 K upon the continuous change of static B_{DC} field in the range 0 – 1 T; ***b***) field dependency of the relaxation time at 2 K fitted to direct process; ***c***) ln τ vs 1/T dependencies obtained from dynamic magnetic investigation of **1** at 0.05 T, 0.06 T and 0.07 T DC fields. The solid lines represent the fits to the combination of direct and Orbach relaxation mechanisms and dashed lines present Orbach fits in the temperature range 3.3 K-4.9 K.

The temperature-dependent dynamic magnetic investigation was recorded at three static fields $B_{DC} = 0.05$ T, 0.06 T, and 0.07 T where the SRM lasted for the longest (Figure 7b, Table S4). Frequency-dependent in-phase χ' and out-of-phase susceptibility χ'' measured as a function of the frequency of AC field for a set of temperatures (1.9-4.9 K, Figures S14-S16 and Tables S5-S7, see ESI) suggest a single relaxation process. At all three fields, the out-of-phase components χ'' shows the maximum shift from 5.7 Hz (at 1.9 K, $\tau \approx 28$ ms) towards higher frequencies upon the increase of the temperature. This indicates the typical feature of SMMs - the maxima of χ'' are frequency and

temperature dependent and the relaxation time τ shortens with the increase of temperature. The temperature-dependent AC susceptibility measurements were fitted using an extended one-set Debye, which enabled us to obtain the relaxation time τ at corresponding temperatures and static magnetic fields. The analysis of lnτ vs 1/T dependences at three fields 0.05 T, 0.06 T, and 0.07 T has been carried out with respect to relaxation equation (3) involving the terms of direct, Raman and Orbach relaxation mechanisms, respectively

$$\frac{1}{\tau} = aTH^m + CT^n + \frac{1}{\tau_0}\exp(-\frac{U_{\text{eff}}}{kT}) \quad (3)$$

where the pre-exponential factor C of the Raman process can be expressed by equation (3)

$$C = d\left(\frac{1+eH^2}{1+fH^2}\right) \quad (4)$$

The comprehensive analysis that involved all three relaxation mechanisms participating on SRM was performed with fixed aH^m and C parameters (Table S9, Figure S17a), calculated by eq (4) using previously obtained parameters a, m, d, e, and f (*vide supra*, Table S8). The fitted values of Orbach effective energy barrier U_{eff} and Raman exponent n slightly decrease upon the increase of DC field from $U_{\text{eff}} = 42$ K and $n = 5.8$ at 0.05 T up to $U_{\text{eff}} = 36$ K and $n = 4.5$ at 0.07 T. On the other hand, the same fitting approach with all free parameters led to DC field invariant values of $U_{\text{eff}} \approx 25$ K, $\tau_0 \approx 1\times10^{-6}$ s, $aH^m \approx 17.4$ s^{-1} while the Raman parameters changing in narrow ranges $C = 0.3\times10^{-3}$–3×10^{-3} K^{-n} s^{-1} and $n = 9.4 - 12$, respectively (Table S10, Figure S17b).

The reliable results also afforded the combination of direct relaxation with either Orbach or Raman process (Figure 7c, Figure S18 and S19). Both combinations resulted in the field invariant parameters $U_{\text{eff}} \approx 32$ K; $\tau_0 \approx 6\times10^{-8}$ s; $aH^m \approx 22$ s^{-1} (direct & Orbach, Table S11); $C \approx 32$ K; $n \approx 8.7$ and $aH^m \approx 1522$ s^{-1} (direct & Raman, Table S12). It is worth noting that the energy barrier of spin reversal obtained from direct & Orbach analysis is close to the one observed from the linear fit of the high-temperature region (3.3 K to 4.9 K), where the only single Orbach relaxation was considered (Figure 7c, dashed lines). Furthermore, the Raman exponent from direct & Raman fit is very close to the theoretically expected value for Kramers ions.

The effective energy barrier U_{eff} for **1** obtained from the analysis of three lnτ vs 1/T temperature dependencies aiming the various combinations of relaxation mechanisms vary in the range 24 cm^{-1} - 42 cm^{-1} and in each case is significantly smaller than the calculated energy gap between the ground and first doublets (*vide supra*). Furthermore, observed values can be compared with U_{eff} of similar five-coordinated Co(II)-SMMs systems with tridentate derivatives of bis(1*H*-benzimidazole-2-yl)pyridine organic ligands and Cl^- or Br^- halido terminal ligands (Table S13). The overview clearly indicates, that complexes containing the unsubstituted bis(1*H*-benzimidazole-2-yl)pyridine[13] or ligands substituted with aromatic 3,5-di-tert-butylbenzyl substituents[12] possess notably smaller U_{eff} comparing to herein reported system **1** or to the complexes containing aliphatic n-octyl or n-dodecyl

substituents[11] attached to the bis(1*H*-benzimidazole-2-yl)pyridine moiety. This lead us to the cautious conclusion that increasing σ-donor character of bis(1*H*-benzimidazole-2-yl)pyridine ligand, induced by strong inductive effect of the attached long aliphatic chains, may have an impact on the effective energy barrier of the spin reversal in five-coordinate Co(II)-SMMs.

Conclusion

In summary, we have prepared a novel tridentate ligand - 2,6-bis(bezimidazole-1*H*-yl)pyridine derivative decorated by the aliphatic n-decyl substituents which has been used for the synthesis of mononuclear pentacoordinated complex **1**. The structural study revealed square-pyramidal geometry of coordination polyhedron and Hirshfeld surface analysis allowed to investigate several non-covalent contacts between C-H hydrogen atoms and bromide anions or between neighboring aromatic moieties of tridentate ligands.

The *ab initio* calculations levels revealed an orbitally degenerate ground electronic state (^{4}E) stemming from C_{4v} ligand field that precludes to use the spin Hamiltonian to describe the magnetic properties of the investigated system. Thus, the analysis of CASSCF/DLPNO-NEVPT2 calculations was based on L-S Hamiltonian and revealed the easy axis type of the magnetic anisotropy. Moreover, these calculations provided valuable information for other experimental techniques studying magnetic and spectroscopic properties. Indeed, the L-S Hamiltonian was successfully applied for the fitting of the static magnetic properties and far-infrared magnetic spectroscopy data, whereas X-band EPR was focusing on the properties of the ground state Kramers doublet. X-band EPR study revealed that the observed effective *g*-factors and hyperfine couplings of the ground Kramers doublet are well described by the Angular Overlap model predictions, while CASSCF-NEVPT2 calculations using quasi-degenerate perturbation theory seem to overestimate their anisotropy in the case of pentacoordinated central Co(II). All employed techniques resulted in a unique match of crystal field parameters, spin-orbit coupling constants, and orbital reduction factors, and all obtained values are comparable with similar pentacoordinated Co(II) SMMs. FIRMS spectra provide a direct experimental measurement of the separation between the ground and first excited states.

The AC susceptibility investigation proved the presence of single-channel SRM at the applied static magnetic field. The DC field-dependent dynamic magnetic investigation at $T = 2$ K revealed that SRM is accomplished by the combination of direct and Raman relaxation mechanisms, while the relaxation upon the increase of temperature is governed either by a complex combination of two (direct & Orbach or direct & Raman) or all three (direct & Raman & Orbach) relaxation mechanisms. The experimental energy barrier obtained from various fits spans in the narrow range from 24 cm^{-1} up to 42 cm^{-1} and in each case is significantly smaller than the calculated energy gap between the ground and first doublets, which is often observed in other Co(II)-SIMs.

Acknowledgement

Grant Agencies (Slovakia: APVV-18-0197, APVV-18-0016, APVV-19-0087, VEGA 1/0029/22; Czech republic: GAČR 22-23760S) are acknowledged for the financial support. This article was written thanks to the generous support under the Operational Program Integrated Infrastructure for the project: "Strategic research in the field of SMART monitoring, treatment and preventive protection against coronavirus (SARS-CoV-2) ", Project no. 313011ASS8, co-financed by the European Regional Development Fund. R.H. and I.Š. acknowledge the financial support from institutional sources of the Department of Inorganic Chemistry, Palacký University Olomouc, Czech Republic.

References

(1) Thiele, S.; Balestro, R.; Klyatskaya, S.; Ruben, M.; Wernsdorfer, W. Electrically driven nuclear spin resonance in single-molecule magnets. *Science* **2014**, *344*, 1135-1138.
(2) Vincent, R.; Klyatskaya, S.; Ruben, M.; Wernsdorfer, W.; Balestro, F. Electronic read-out of a single nuclear spin using a molecular spin transistor. *Nature* **2012**, *488*, 357–360.
(3) Ding, Y.-S.; Chilton, N. F.; Winpenny R. E. P.; Zheng, Y.-Z. On Approaching the Limit of Molecular Magnetic Anisotropy: A Near-Perfect Pentagonal Bipyramidal Dysprosium(III) Single-Molecule Magnet. *Angew. Chem., Int. Ed.* **2016**, *55*, 16071–16074.
(4) ed. Layfield, R. A.; Murugesu, M. *Lanthanides and Actinides in Molecular Magnetism*, Wiley-VCH Verlag GmbH & Co. KGaA, Weinheim, 2015.
(5) Frost, J. M.; Harriman K. L. M.; Murugesu, M. The rise of 3-d single-ion magnets in molecular magnetism:towards materials from molecules? *Chem. Sci.* **2016**, *7*, 2470 – 2491.
(6) Juráková, J.; Šalitroš, I. Co(II) single-ion magnets: synthesis, structure, and magnetic properties. Monatsh. Chem. **2022** *153*, 1001–1036.
(7) Nemec, I.; Herchel, R.; Kern, M.; Neugebauer, P.; van Slageren, J.; Travnicek, Z. Magnetic Anisotropy and Field-induced Slow Relaxation of Magnetization in Tetracoordinate Co-II Compound [Co(CH3-im)(2)Cl-2]. *Materials* **2017** *10*, 249.
(8) Ghosh, S.; Kamilya, S.; Das, M.; Mehta, S.; Boulon, M. E.; Nemec, I.; Rouzieres, M.; Herchel, R.; Mondal, A. Effect of Coordination Geometry on Magnetic Properties in a Series of Cobalt(II) Complexes and Structural Transformation in Mother Liquor. *Inorg. Chem.* **2020**, *59*, 7067-7081.
(9) Jurca, T.; Farghal, A.; Lin, P. H.; Korobkov, I.; Murugesu, M.; Richeson, D. S. J. Single-Molecule Magnet Behavior with a Single Metal Center Enhanced through Peripheral Ligand Modifications. *J. Am. Chem. Soc.*, **2011**, *133*, 15814–15817.
(10) Habib, F.; Luca, O. R.; Vieru, V.; Shiddiq, M.; Korobkov, I.; Gorelsky, S. I.; Takase, M. K.; Chibotaru, L. F.; Hill, S.; Crabtree, R. H.; Murugesu, M. Influence of the Ligand Field on Slow Magnetization Relaxation versus Spin Crossover in Mononuclear Cobalt Complexes. *Angew. Chem. Int. Ed.* **2013**, *52*, 11290 –11293.
(11) Juráková, J.; Midlíková, J. D. M.; Hrubý, J.; Kliuikov, A.; Santana, V. T.; Pavlik, J.; Moncoľ, J.; Čižmár, E.; Orlita, M.; Mohelský, I.; Neugebauer, P. Gentili, D.; Cavallini, M.; Šalitroš, I. Pentacoordinate cobalt(II) single ion magnets with pendant alkyl chains: shall we go for chloride or bromide? *Inorg. Chem. Front.*, **2022**, *9*, 1179-1194.
(12) Brachňaková, B.; Matejová, S.; Moncol, J.; Herchel, R.; Pavlik, J.; Moreno-Pineda, E.; Ruben, M.; Šalitroš, I. Stereochemistry of coordination polyhedra vs. single ion magnetism in penta- and hexacoordinated Co(II) complexes with tridentate rigid ligands. *Dalton Trans.*, **2020**, *49*, 1249–1264.
(13) Mondal, A. K.; Goswami, T.; Misra, A.; Konar, S. Probing the Effects of Ligand Field and Coordination Geometry on Magnetic Anisotropy of Pentacoordinate Cobalt(II) Single-Ion Magnets. *Inorg. Chem.* **2017**, *56*, 6870–6878.
(14) Boča, R. Magnetic Functions Beyond the Spin-Hamiltonian. *Struct. Bond.* **2006** *117*, 1-264.
(15) Addison, A.; Burke., P. Synthesis of Some Imidazole- and Pyrazole- Derived Chelating Agents. J. Heterocycl. Chem. 1981. 18. 803–805.

(16) Koziskova, J.; Hahn, F.; Richter, J.; Kozisek, J. Comparison of different absorption corrections on the model structure of tetrakis(μ 2-acetato)-diaqua-di-copper(II). *Acta Chim. Slovaca* **2016**, *9*, 136–140.
(17) Palatinus, L.; Chapuis, G. SUPERFLIP - A computer program for the solution of crystal structures by charge flipping in arbitrary dimensions. *J. Appl. Crystallogr.* **2007**, *40*, 786–790.
(18) Sheldrick, G. M. Crystal structure refinement with *SHELXL*. *Acta Crystallogr.* **2015**, *C71*, 3–8.
(19) Dolomanov, O. V.; Bourhis, L. J.; Gildea, R. J.; Howard, J. A. K.; Puschmann, H. OLEX2: A complete structure solution, refinement and analysis program. *J. Appl. Crystallogr.* **2009**, *42*, 339–341.
(20) Spackman, P. R.; Turner, M. J.; McKinnon, J. J.; Wolff, S. K.; Grimwood, D. J.; Jayalitaka, D.; Spackman, M. A. *CrystalExplorer*: a program for Hirshfeld surface analysis, visualization and quantitative analysis of molecular crystals. *J. Appl. Crystallogr.* **2021**, *54*, 1006–1011.
(21) Spackman, M. A.; Jayalitaka, D. Hirhfeld surface analysis. *CrystEngComm* **2009**, *11*, 19–32.
(22) McKinnon, J. J.; Spackman, M. A.; Mitchell, A. S. Novel tools for visualizing and exploring intermolecular interactions in molecular crystals. *Acta Crystallogr.* **2004**, *B60*, 627–668.
(23) Spackman, M. A.; Mckinnon, J. J.; Jayalitaka, D. Electrostatic potentials mapped on Hirshfeld surfaces provide direct insight into intermolecular interactions in crystals. *CrystEngComm* **2008**, *10*, 368–376.
(24) Spackman, M. A.; McKinnon, J. J. Fingerprinting intermolecular interactions in molecular crystals. *CrystEngComm* **2002**, *4*, 378–392.
(25) Parkin, A.; Barr, G.; Dong, W.; Gilmore, C. J.; Jayalitaka, D.; McKinnon, J. J.; Wilson, C. C. Comparing entire crystal structures: structural genetic fingerprinting. *CrystEngComm* **2007**, *9*, 648–652.
(26) McKinnon, J. J.; Jayalitaka, D.; Spackman, M. A. Spackman, Towards quantitative analysis of intermolecular interactions with Hirshfeld surfaces. *Chem. Commun.* **2007**, 3814–3816.
(27) R. Boča. Theoretical Foundations of Molecular Magnetism. Elsevier. Amsterdam. 1999.
(28) Malmqvist, P.Å.; Roos, B.O. The CASSCF State Interaction Method. *Chem. Phys. Lett.* **1989**, *155*, 189–194, doi:10.1016/0009-2614(89)85347-3.
(29) Y. Guo, K. Sivalingam, E. F. Valeev and F. Neese, *J. Chem. Phys.*, **2017**, *147*, 064110.
(30) https://wires.onlinelibrary.wiley.com/doi/full/10.1002/wcms.1606 and https://aip.scitation.org/doi/full/10.1063/5.0004608
(31) C. F. Macrae, I. Sovago, S. J. Cottrell, P. T. A. Galek, P. McCabe, E. Pidcock, M. Platings, G. P. Shields, J. S. Stevens, M. Towler and P. A. Wood, J. Appl. Cryst., 53, 226-235, 2020
(32) C. van Wüllen, *J. Chem. Phys.*, **1998**, *109*, 392.
(33) F. Weigend and R. Ahlrichs, Phys. Chem. Chem. Phys. 7, 3297 (2005).
(34) F. Weigend, Phys. Chem. Chem. Phys. 8, 1057 (2006)
(35) Stoychev, G. L.; Auer, A. A.; Neese, F. (**2017**) *J. Chem. Theory Comput.*, 13(2), 554.
(36) Izsák, R.; Neese, F. An Overlap Fitted Chain of Spheres Exchange Method. *J. Chem. Phys.* **2011**, *135*, 144105, doi:10.1063/1.3646921.
(37) Neese, F.; Wennmohs, F.; Hansen, A.; Becker, U. Efficient, Approximate and Parallel Hartree–Fock and Hybrid DFT Calculations. A 'Chain-of-Spheres' Algorithm for the Hartree–Fock Exchange. *Chem. Phys.* **2009**, *356*, 98–109, doi:10.1016/J.CHEMPHYS.2008.10.036.
(38) Mingos, D. M. P.; Day, P.; Dahl, J. P. Molecular Electronic Structures of Transition Metal Complexes II. Springer **2012**, *143*, doi:10.1007/978-3-642-27378-0.
(39) Singh, S.K.; Eng, J.; Atanasov, M.; Neese, F. Covalency and Chemical Bonding in Transition Metal Complexes: An Ab Initio Based Ligand Field Perspective. *Coord. Chem. Rev.* **2017**, *344*, 2–25, doi:10.1016/J.CCR.2017.03.018.
(40) Boca, R. Zero-field splitting in metal complexes, *Coord. Chem. Rev.* **2004**, 248(9), 757-815.
(41) Figgis, B.N.; Gerloch, M.; Lewis, J.; Mabbs, F.E.; Webb, G.A. The Magnetic Behaviour of Cubic-Field 4T1g Terms in Lower Symmetry. *J. Chem. Soc. A.* **1968**, *57*, 2086–2093, doi:10.1039/J19680002086.
(42) Griffith, J.S. The Theory of Transition-Metal Ions; Cambridge University Press&Assessment: Cambridge; Great Britain; 2009; pp. 455.

(43) Mingos, D.M.P. Magnetic Functions Beyond the Spin-Hamiltonian 2006, Springer Berling Heidelberg: Berlin, Germany, 2006, pp. 278.
(44) Boča, R. A Handbook of Magnetochemical Formulae; 2012, Elsevier: Amsterdam, The Netherlands, pp. 1010.
(45) Herchel, R.; Boča, R. Program Polymagnet; Slovak Technical University: Bratislava, Slovakia, 2006–2021.
(46) Nemec, I.; Herchel, R.; Travníček, Z. *Dalton Trans.* **2018**, *47*, 1614−1623
(47) Zoufalý, P.; Kliuikov, A.; Čižmár, E.; Císařová, I.; Herchel, R. Cis and Trans Isomers of Fe(II) and Co(II) Complexes with Oxadiazole Derivatives - Structural and Magnetic Properties. *Eur. J. Inorg. Chem.* **2021**, 1190–1199, doi:10.1002/EJIC.202001148.
(48) Drahoš, B.; Šalitroš, I.; Císařová, I.; Herchel, R. A Multifunctional Magnetic Material Based on a Solid Solution of Fe(II)/Co(II) Complexes with a Macrocyclic Cyclam-Based Ligand. *Dalton Trans.* **2021**, *50*, 11147–11157, doi:10.1039/D1DT01534F.
(49) Ghosh, S.; Kamilya, S.; Rouzières, M.; Herchel, R.; Mehta, S.; Mondal, A. Reversible Spin-State Switching and Tuning of Nuclearity and Dimensionality via Nonlinear Pseudohalides in Cobalt(II) Complexes. *Inorg. Chem.* **2020**, *59*, 17638–17649, doi:10.1021/ACS.INORGCHEM.0C02887.
(50) Nemec, I.; Fellner, O.F.; Indruchová, B.; Herchel, R. Trigonally Distorted Hexacoordinate Co(II) Single-Ion Magnets. *Materials* **2022**, *15*, 1064.
(51) Maurice, R.; Bastardis, R.; Graaf, C.; Suaud, N.; Mallah, T.; Guihery, N.́ *J. Chem. Theory Comput.* **2009**, *5*, 2977−2984.
(52) Chibotaru, L.F.; Ungur, L. Ab Initio Calculation of Anisotropic Magnetic Properties of Complexes. I. Unique Definition of Pseudospin Hamiltonians and Their Derivation. *J. Phys. Chem*. **2012**, *137*, 064112, doi:10.1063/1.4739763
(53) Dey, A.; Kalita, P.; Chandrasekhar, V. Lanthanide(III)-Based Single-Ion Magnets. *ACS Omega* **2018**, *3*, 9462–9475, doi:10.1021/ACSOMEGA.8B01204.
(54) Vallejo, J.; Castro, I.; Ruiz-Garcia, R.; Cano, J.; Julve, M.; Lloret, F.; De Munno, G.; Wernsdorfer, W.; Pardo, E. Field-Induced Slow Magnetic Relaxation in a Six-Coordinate Mononuclear Cobalt(II) Complex with a Positive Anisotropy. *J. Am. Chem. Soc.* **2012**, *134*, 38, 15704–15707.
(55) Herchel, R.; Váhovská, L.; Potočňák, P.; Trávníček, Z. *Inorg. Chem.* **2014**, *53*, 5896−5898.
(56) Stoll, S.; Schweiger, A. EasySpin, a comprehensive software package for spectral simulation and analysis in EPR. *J. Magn. Res.* **2006**, *178*, 42–55.
(57) Suturin, E. A.; Nehrkorn, J.; Zadrozny, J. M.; Liu, J.; Atanasov, M.; Weyhermüller, T.; Maganas, D.; Hill, S.; Schnegg, A.; Bill, E.; Long, J. R.; Neese, F. Magneto-Structural Correlations in Pseudotetrahedral Forms of the [Co(SPh)4]2– Complex Probed by Magnetometry, MCD Spectroscopy, Advanced EPR Techniques, and ab Initio Electronic Structure Calculations. *Inorg. Chem.* **2017**, *56*, 5, 3102–3118.
(58) Banci L., Bencini A., Benelli C., Gatteschi D., Zanchini C. (1982) Spectral-structural correlations in high-spin cobalt(II) complexes. In: Structures versus Special Properties. Structure and Bonding, vol 52. Springer, Berlin, Heidelberg.
(59) Shrivastava, K. N. Theory of Spin–Lattice Relaxation. *Phys. Status Solidi B* **1983**, 117, 437–458.